Supporting Information

Toward Highly Efficient Protonic Electrolysis Cells for Large-scale Hydrogen Production at Moderate Temperatures

Kwati Leonard [1, 3, 4], * Kuninori Miyazaki [2], Christian Dellen [3], Mariya E. Ivanova[3], Wendelin Deibert [3], Julia Wolter [3], Wilhelm A. Meulenberg [3], Olivier Guillon[3], Veeramani Vediyappan[4], Tatsumi Ishihara[1,4], and Hiroshige Matsumoto[1,4]

[1]*Center for Energy Systems Design (CESD), International Institute for Carbon Neutral Energy Research (WPI-I2CNER), Kyushu University744 Motooka, Nishiku, Fukuoka 819-0395, Japan*

[2] *Strategic Institute of Technology and Research Center, 992-1 Nishioki, Himeji, Hyogo 671-1292*

[3] *Institute of Energy Materials and Devices (IMD) Materials Synthesis and Processing (IMD-2), Forschungszentrum Jülich GmbH, Wilhelm-Johnen-Straße 52428 Germany*

[4]*International Institute for Carbon Neutral Energy Research (WPI-I2CNER), Kyushu University744 Motooka, Nishiku, Fukuoka 819-0395, Japan*

***Correspondence:**

kwati@i2cner.kyushu-u.a.jp; Tel.: +81-092-802-6706

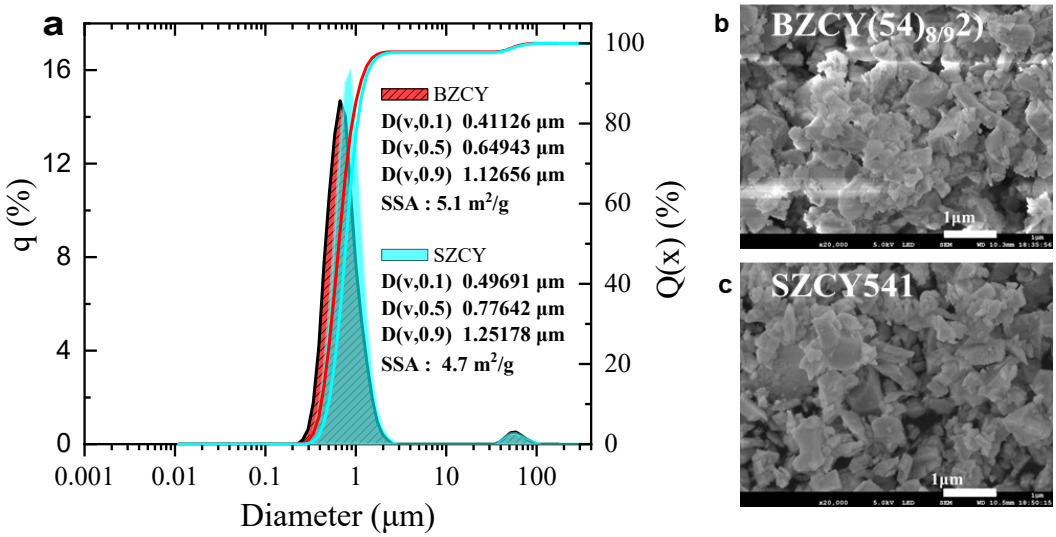

Figure S1. (a) Particle size distributions after a two-step calcination process at 900 and 1200 °C and subsequent ball milling of the precursor powders. (b) $BaZr_{0.44}Ce_{0.36}Y_{0.2}O_{3-\delta}$ powder (c) $SrZr_{0.5}Ce_{0.4}Y_{0.1}O_{3-\delta}$ (SZCY541) powder

Table S1. A comprehensive summary of the tape-casting parameters, adjusted casting speed, and blade gaps utilized for the fabrication of the half-cells.

Layer	Blade gap [µm]	Casting speed [mm/s]	Drying time [h]	Green thickness[µm]	End fired thickness[µm]	Investigation
Electrolyte						
Electrolyte 1	70	5	5	15.4	~10	Half-cell
Electrolyte 2	65	5	5	13.4	~8	Half-cell
Substrate and functional layer (CFL)						
CFL	40	10	5	10	~8	Half-cell
Substrate	1200	2.5	~10 - 12	602	~450-520	Half-cell

Table S2. Summary of the components utilized to formulate the ceramic protonic slurry for tape casting.

Slurry components	Powder	Pore Former	Solvent	Dispersing Agent	Binder
Materials	$BaZr_{0.44}Ce_{0.36}Y_{0.2}O_{3-\delta}$ $NiO\text{-}SrZr_{0.5}Ce_{0.4}Y_{0.1}O_{3-\delta}$	Potato starch	Ethanol/MEK	Nuosperse FX 9086	PVB-98
Plasticizer	+ Plasticizer Type I Solusolv S-2075			+ Plasticizer Type II PEG 400	

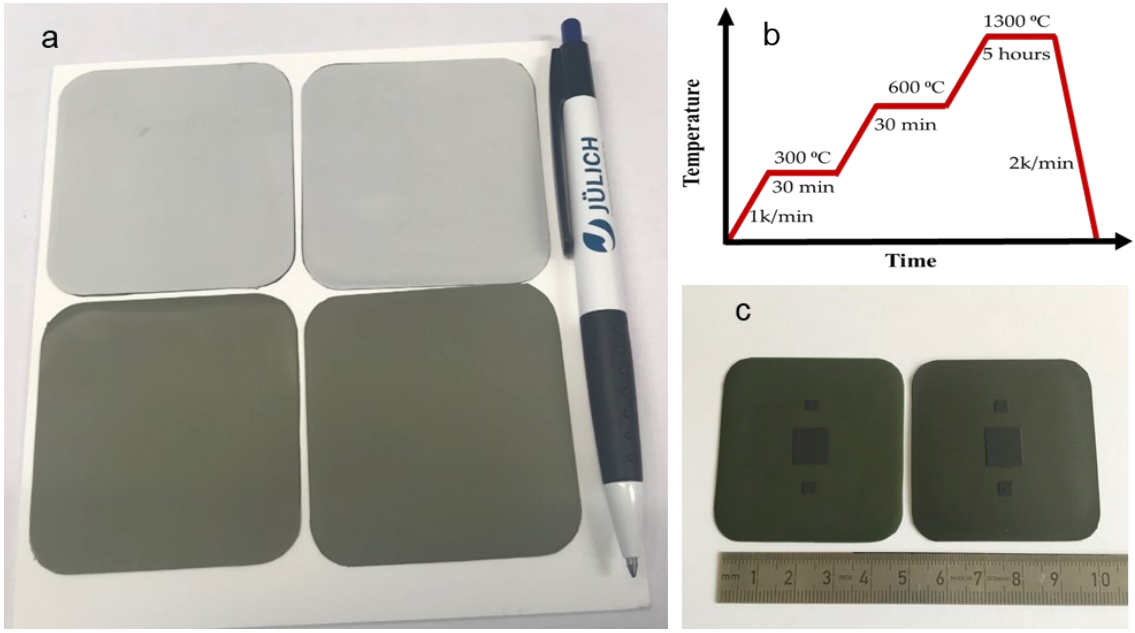

Figure S2. a) Sequentially cast and cut out $BaZr_{0.44}Ce_{0.36}Y_{0.2}O_{3-\delta}$, green tapes, consisting of a thin $BaZr_{0.44}Ce_{0.36}Y_{0.2}O_{3-\delta}$, electrolyte layer and a $NiO\text{-}SrZr_{0.5}Ce_{0.4}Y_{0.1}O_{3-\delta}$ functional and substrate layer b) Temperature program applied for sintering the planar half-cells in the present study. (c) Typical 5 x 5 cm^2 half-cells after sintering with the air electrode applied.

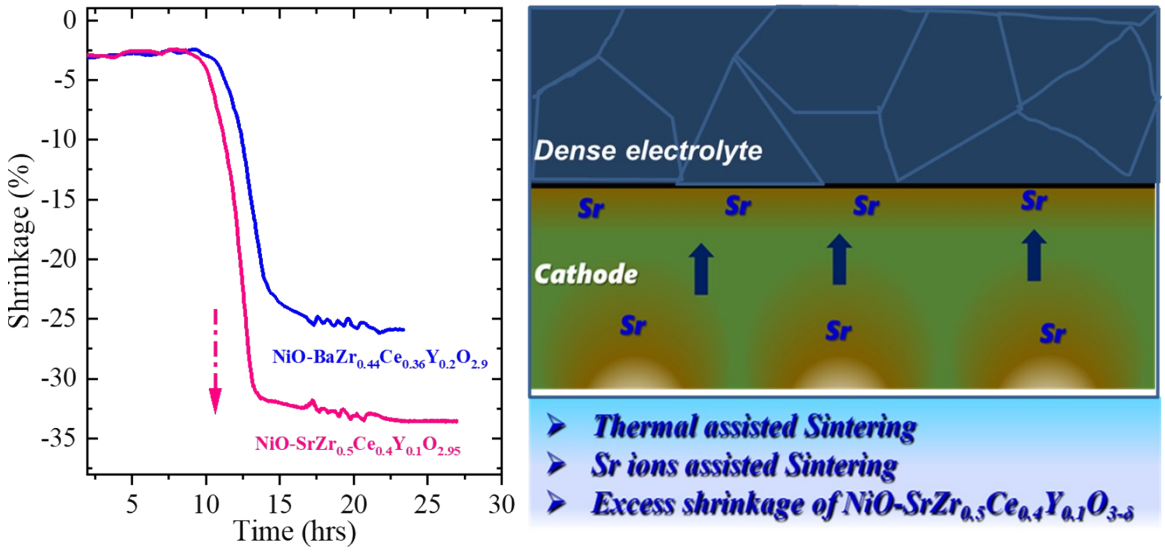

Figure S3. Shrinkage behavior comparison of $BaZr_{0.44}Ce_{0.36}Y_{0.2}O_{3-\delta}$,|NiO-$BaZr_{0.44}Ce_{0.36}Y_{0.2}O_{3-\delta}$, and $BaZr_{0.44}Ce_{0.36}Y_{0.2}O_{3-\delta}$,|NiO-$SrZr_{0.5}Ce_{0.4}Y_{0.1}O_{3-\delta}$ bi-layers determined by optical dilatometry**,** Schematic illustration of strontium ions streaming towards the electrolyte layer and possible assisting densification of $BaZr_{0.44}Ce_{0.36}Y_{0.2}O_{3-\delta}$, electrolyte.

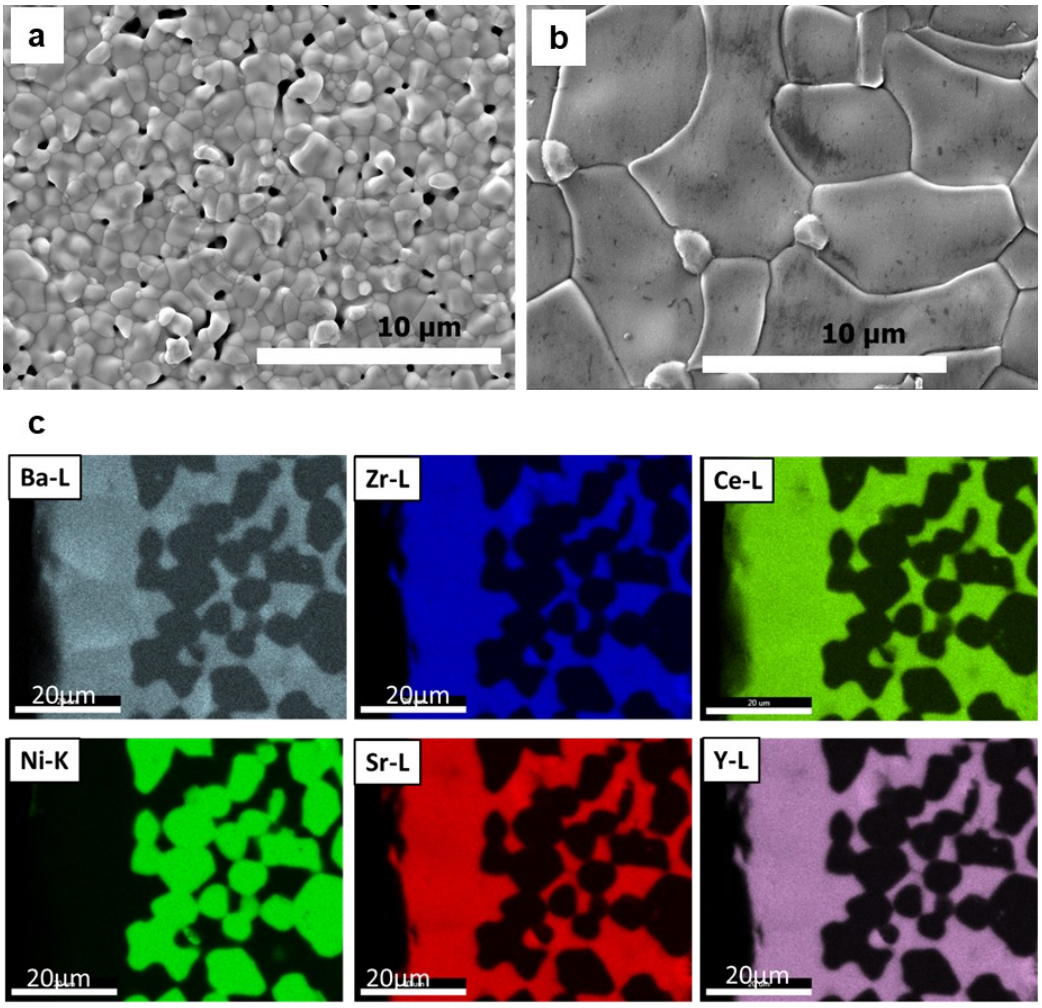

Figure S4. SEM image of $BaZr_{0.44}Ce_{0.36}Y_{0.2}O_{3-\delta}$ surface on a) NiO-$BaZr_{0.44}Ce_{0.36}Y_{0.2}O_{3-\delta}$, electrode and on b) NiO-$SrZr_{0.5}Ce_{0.4}Y_{0.1}O_{3-\delta}$ after sintering at 1350 °C/5h. (c) SEM image of a polished cross-section of the $BaZr_{0.44}Ce_{0.36}Y_{0.2}O_{3-\delta}$ / $SrZr_{0.5}Ce_{0.4}Y_{0.1}O_{3-\delta}$ half-cell and the corresponding EDS elemental maps of Ba, Zr, Ce, Y, Sr, and Ni after sintering at 1350 °C/5h.

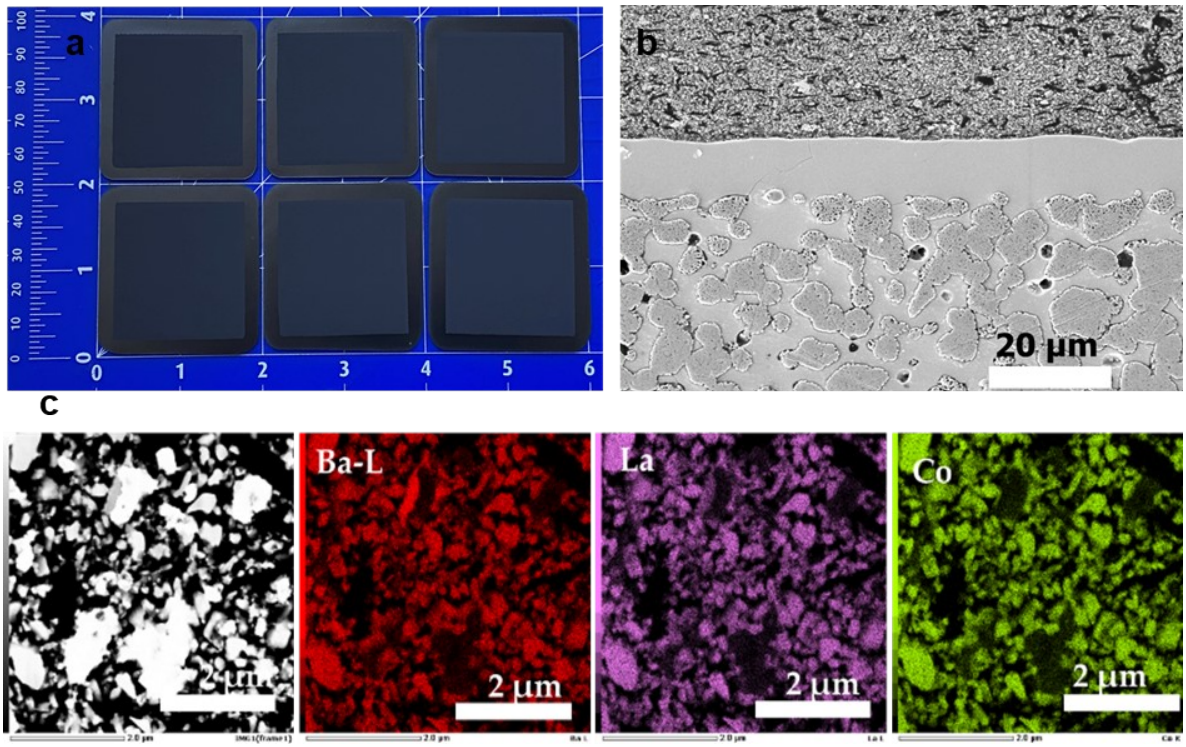

Figure S5. Photograph images of some of the as-fabricated 50 × 50 mm^2 planar $BaZr_{0.44}Ce_{0.36}Y_{0.2}O_{3-\delta}$, based complete cells with a 1600 mm^2 steam electrode, on NiO-$SrZr_{0.5}Ce_{0.4}Y_{0.1}O_{3-\delta}$ substrate (b) The microstructure, post cell measurement (c) HADDF image of $Ba_{0.5}La_{0.5}CoO_3$ electrode after firing at 800°C.

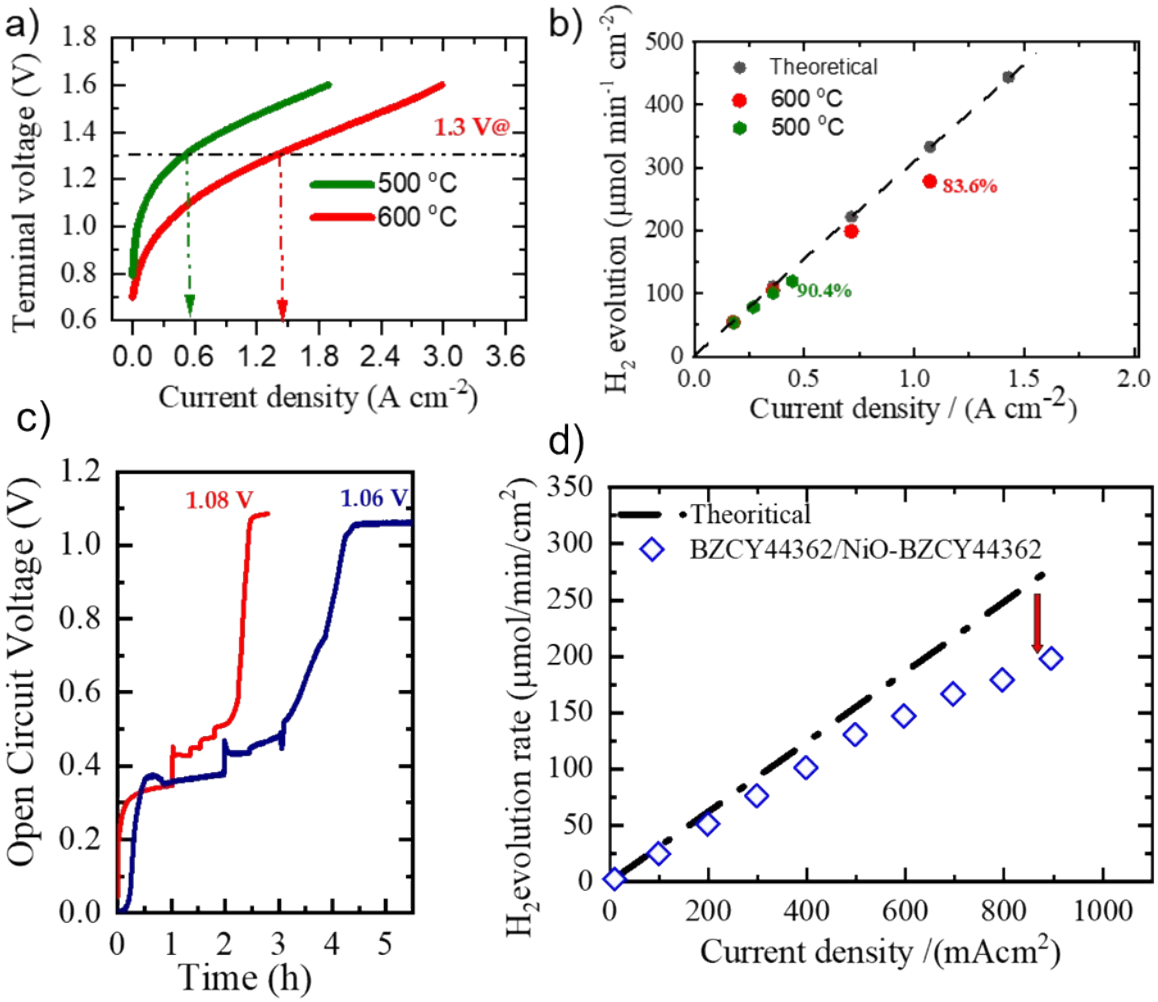

Figure S6. I–V characteristic of the as-fabricated $BaZr_{0.44}Ce_{0.36}Y_{0.2}O_{3-\delta}$, steam electrolysis-based cell on a NiO-$SrZr_{0.5}Ce_{0.4}Y_{0.1}O_{3-\delta}$ substrate and b) the generated hydrogen measured at 500, and 600 °C on a 22 mm diameter cell. c) Reduction profile of the BZCY44362|NiO-BZCY44362 red and BZCY44362|NiO-BZCY44362 single cell deep blue. d) Hydrogen generated from BZCY44362|NiO-BZCY44362 based cell

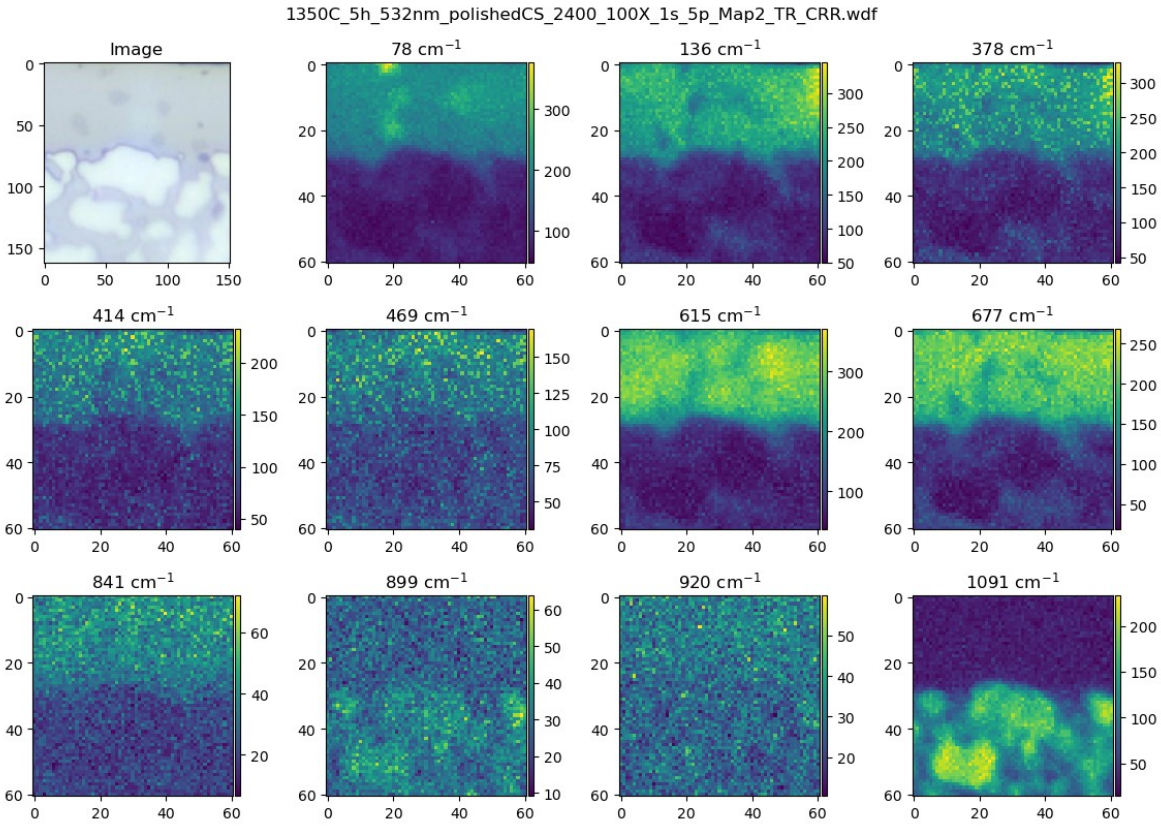

Figure S7. Peak mappings across the $BaZr_{0.44}Ce_{0.36}Y_{0.2}O_{3-\delta}$,|NiO-$SrZr_{0.5}Ce_{0.4}Y_{0.1}O_{3-\delta}$ half-cell interface sintered at 1350 ºC with a five hours dwelling time, showing the optical image of the mapped area and all the respective Raman peak positions. The mapped area starts from the electrolyte above down to the substrate layer

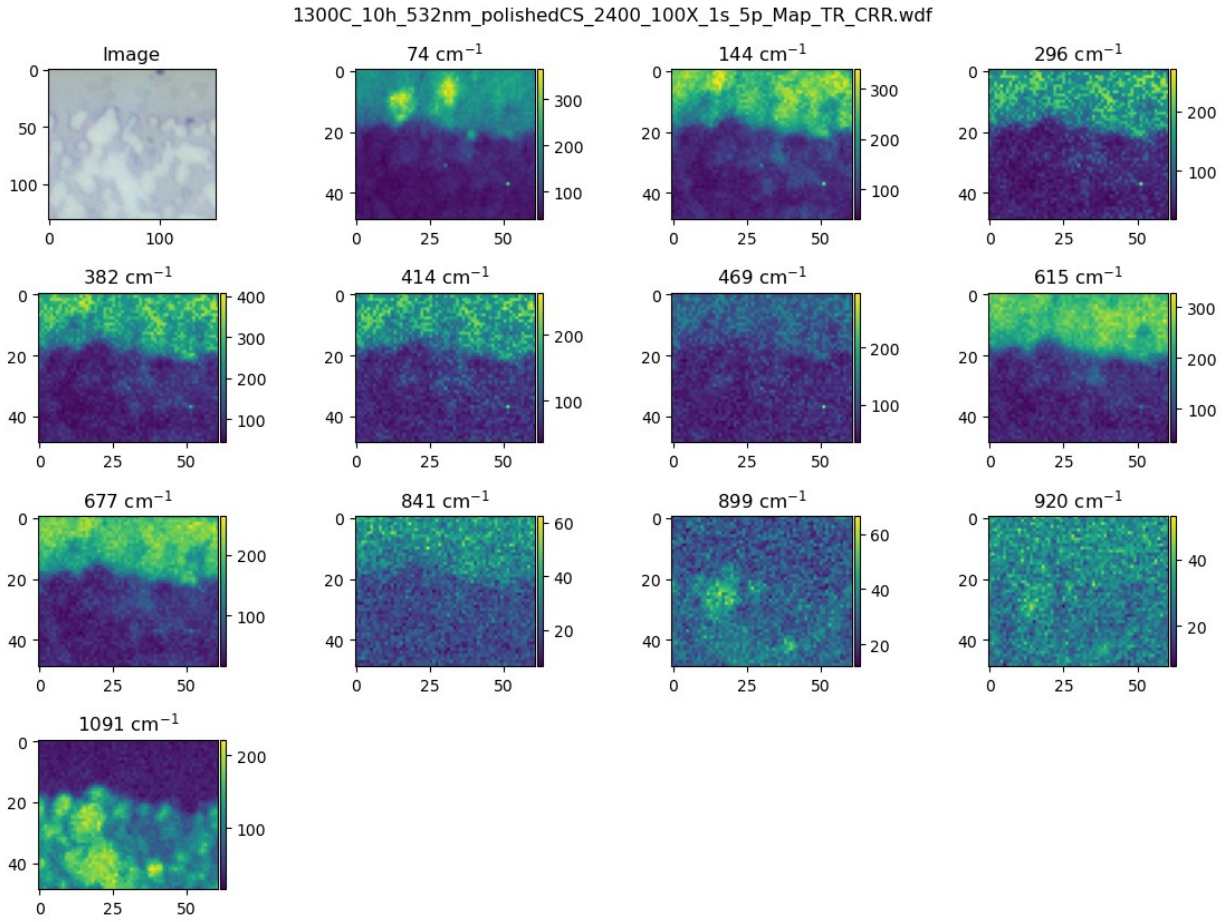

Figure S8. Peak mappings across the $BaZr_{0.44}Ce_{0.36}Y_{0.2}O_{3-\delta}$,|NiO-$SrZr_{0.5}Ce_{0.4}Y_{0.1}O_{3-\delta}$ half-cell interface sintered at 1300 °C with a ten hours dwelling time, showing all the respective Raman peak positions. The mapped area starts from the electrolyte above down to the substrate layer. The optical image of the mapped area is also shown.

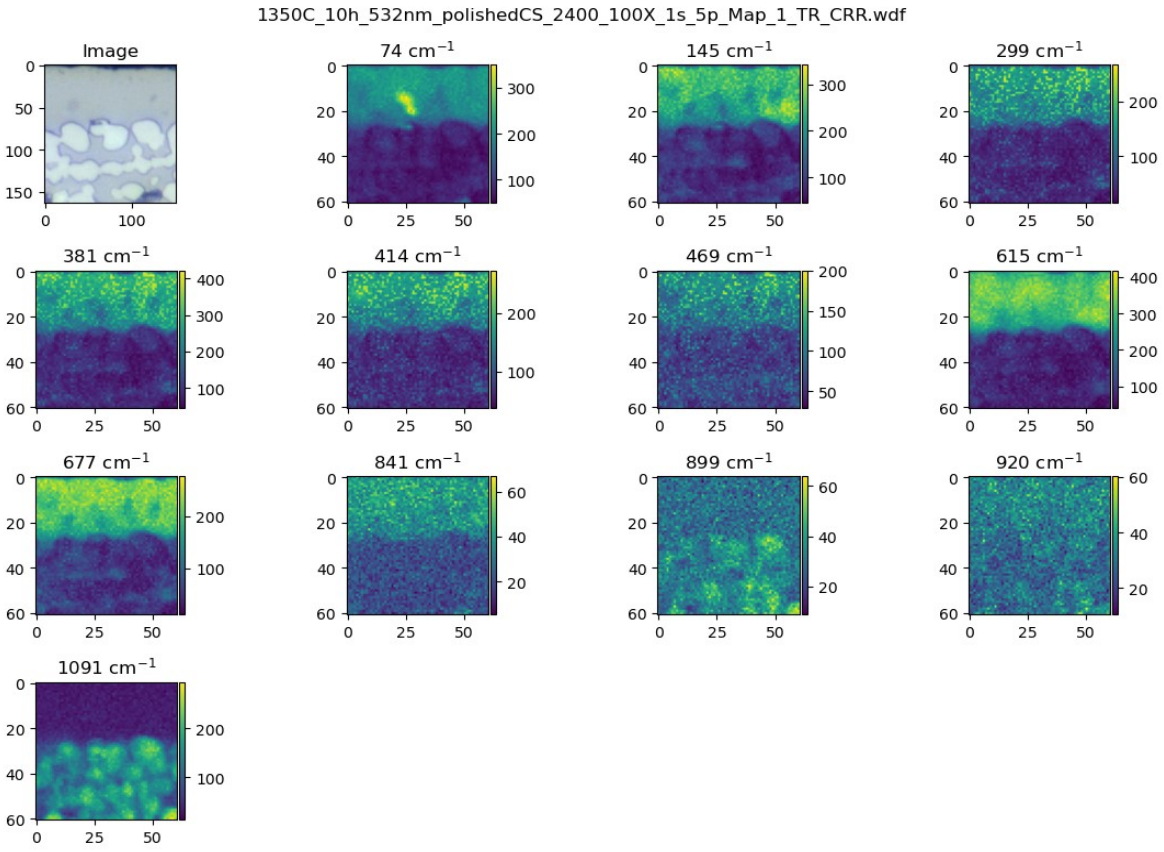

Figure S9. Peak mappings across the $BaZr_{0.44}Ce_{0.36}Y_{0.2}O_{3-\delta}$,|NiO-$SrZr_{0.5}Ce_{0.4}Y_{0.1}O_{3-\delta}$ half-cell interface sintered at 1350 °C with a ten hours dwelling time, showing all the respective Raman peak positions. The mapped area starts from the electrolyte above down to the substrate layer. The optical image of the mapped area is also shown.

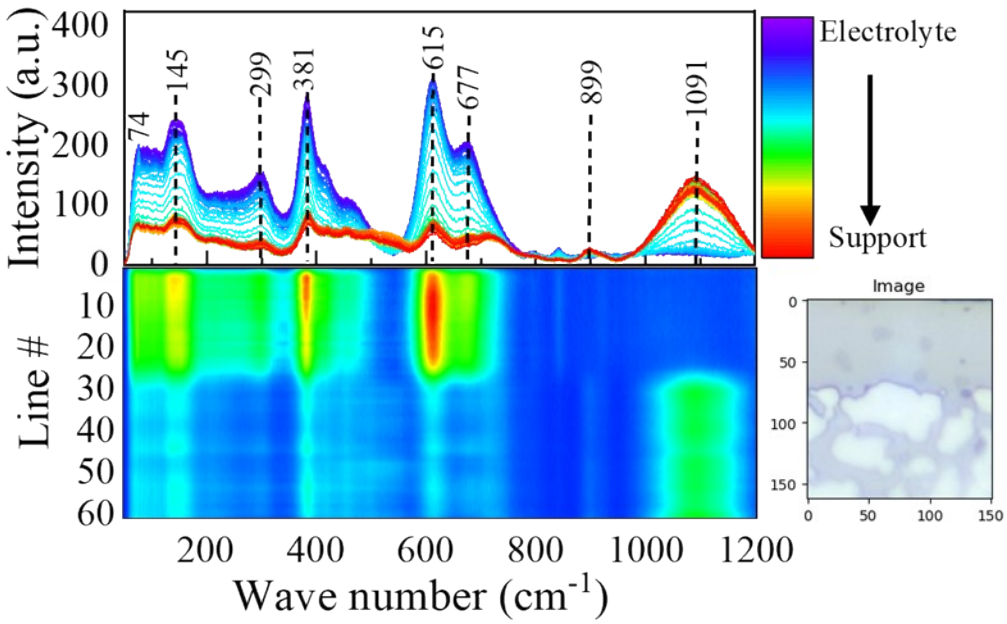

Figure S10. Line averaged Raman spectra obtained from mapped areas on the polished cross-section of the $BaZr_{0.44}Ce_{0.36}Y_{0.2}O_{3-\delta}$,|NiO-$SrZr_{0.5}Ce_{0.4}Y_{0.1}O_{3-\delta}$ half-cell sintered at 1350°C for 10 hours also showing the representative optical image

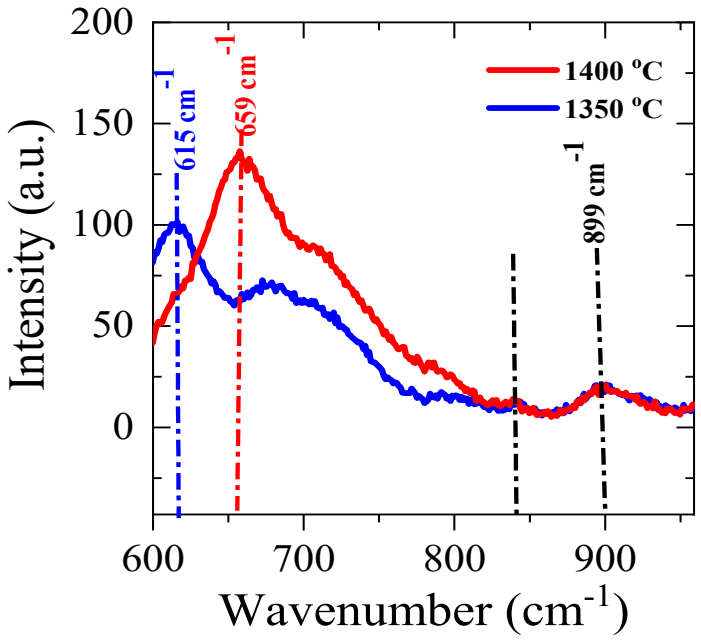

Figure S11. Line averaged Raman spectra obtained from mapped areas on the polished cross-section of the $BaZr_{0.44}Ce_{0.36}Y_{0.2}O_{3-\delta}$,|NiO-$SrZr_{0.5}Ce_{0.4}Y_{0.1}O_{3-\delta}$ half-cell sintered at 1350°C and 1400°C for 5 hours respectively.

Table S3. Comparison of the steam electrolysis performance from this work with some literature reported results.

Reference

	Test condition		Cell performance		
Cell configuration	**Anode gas pressure (electrolyte thickness)**	**Cathode gas pressure**	**J/Acm^{-2} @ 1.3V .temp/°C**	**η_{Fex} %**	**Year [Ref]**
BLC| BZCY(54)$_{8/9}$2| Ni-SZCY541	80% H_2O, 1%O_2 (10µm)	1% H_2 (2% H_2O)	1.37 (600)	83	this work
BLC| BSZCY91(54)$_{8/9}$2| Ni-SZCY541	20% H_2O, 1%O_2 (12µm)	1% H_2 (2% H_2O)	0.5 (600)	90	this work
LSCN|BCZY442|Ni–BCZY442	3% H_2O, air (24) µm	97% H_2 (3% H_2O)	1.09 (600)	N/A	20203[4]
PBCC|BZCYYb1711|Ni- BZCYYb	3% H_2O, O_2 (20) µm	100% H_2	0.72 (600)	N/A	2020[5]
PBCC-BCC|BZCYYb1711|Ni- BZCY	3% H_2O, air (10) µm	H_2 (3% H_2O)	1.51 (600)	N/A	2021[6]
PBSCF|BZCYYb4411|Ni- BZCY	3% H_2O, air (15) µm	97% H_2 (3% H_2O)	1.92 (600)		2019[7]
BSCF-BCZY62|BCZY62|Ni–BCZY	2.8% H_2O, air (15 µm)	50% H_2 (2.8% H_2O)	1.05 (600)	N/A	2013[8]
LSC-BZCYbCo|BZCYbCo|Ni-BZCY	30% H_2O, 19% O2, 45µm	10 % H_2/He	0.03 (600)	85	2011[9]
SEFC-BCZY35|BCZY35|Ni-BCZY	10% H_2O/Air(15µm)	97% H_2 (3% H_2O)	0.42(600)	33	2018[10]
BCZFY|BZCYYb7211|Ni- BZCYYb	20% H_2O, 97% air (5µm)	97% H_2 (3% H_2O)	1.00 (600)	97	2019[11]
PBSCF|BZCYYb411|Ni- BZCYYb	3% H_2O, 97% air (15µm)	97% H_2 (3% H_2O)	1.31(600	75	2019[7]
LNF/LN| BZCD(30µm)|Ni-BZCD	3% H_2O, 97% air (30µm)	97% H_2 (3% H_2O)	0.3 (600)	N/A	2016[12]
SSC-BZCY53|BZCY53|Ni-BZCY53	50% H_2O, 50% air (20µm)	97% H_2 (3% H_2O)	0.33 (600)	…..	2010[13]
SSC-BZCY|BZCY442(15µm)|Pt	20% H_2O, air (1.5mm)	1% H_2 (3% H_2O)	0.04 (600)	70	2018[14]
BLC|BZCY(28)$_8$2|Ni-SZCY541	20% H_2O/1%O_2 (12µm)	1% H_2- 2% H_2O	0.6 (600)	81.5	2022[3]
BLC|BZCY(54)$_{8/9}$2|Ni-SZCY541	20% H_2O/1%O_2 (12µm)	1% H_2- 2% H_2O	0.5 (600)	76.8	2022[3]
PCNfiber|BZCYYb411|Ni- BZCYYb	10% H_2O/Air(15µm)	10% H_2 (3% H_2O)	1.18 (600)		2020[15]
NBSCF-BCZYYb|BCZYYb|Ni-BCZYYb	10% H_2O, air (20µm)	90% H_2 (10% H_2O	0.75 (600)	N/A	2018[16]

BSZCY91(54)$_{8/9}$2=Ba0.9Sr0.1$Zr_{0.44}Ce_{0.36}Y_{0.2}O_{3-\delta}$, BZCY(54)$_{8/9}$2=$BaZr_{0.44}Ce_{0.36}Y_{0.2}O_{3-\delta}$, LSCN=$La_{0.8}Sr_{0.2}Co_{0.7}Ni_{0.3}O_{3-\delta}$

η_{Fex}=Current efficiency, BZY82= $BaZr_{0.8}Y_{0.2}O_{3-\delta}$, SFM=$Sr_2Fe_{1.5}Mo_{0.5}O_{6-\delta}$, BZY = $BaZr_{0.9}Y_{0.1}O_{3-\delta}$, BCZYbCo = $BaCe_{0.48}Zr_{0.40}Yb_{0.10}Co_{0.02}O_{3-\delta}$, BCZD = $BaCe_{0.5}Zr_{0.3}Dy_{0.2}O_{3-\delta}$, BCZY81 = $BaCe_{0.8}Zr_{0.1}Y_{0.1}O_{3-\delta}$, SDC = $Ce_{0.8}Sm_{0.2}O_{2-\delta}$, BCZY44 = $BaCe_{0.4}Zr_{0.4}Y_{0.2}O_{3-\delta}$, BCZYZn = $BaCe_{0.5}Zr_{0.3}Y_{0.16}Zn_{0.04}O_{3-\delta}$, BCZY53 = $BaCe_{0.5}Zr_{0.3}Y_{0.2}O_{3-\delta}$, BSCF= $Ba_{0.5}Sr_{0.5}Co_{0.8}Fe_{0.2}O_{3-\delta}$, NBSCF= $NdBa_{0.5}Sr_{0.5}Co_{1.5}Fe_{0.5}O_{5+\delta}$, LNF/LN= $LaNi_{0.6}Fe_{0.4}O_{3-\delta}$ / $La_2NiO_{4+\delta}$

PBC95=$PrBa_{0.8}Ca_{0.2})_{0.95}Co_2O_{6-\delta}$, PBCC-BCO= $PrBa_{0.8}Ca_{0.2}Co_2O_{5+\delta}$-$BaCoO_{3-\delta}$, PBSCF= $PrBa_{0.5}Sr_{0.5}Co_{1.5}Fe_{0.5}O_{5+\delta}$

(1) Leonard, K.; Lee, Y. S.; Okuyama, Y.; Miyazaki, K.; Matsumoto, H. Influence of Dopant Levels on the Hydration Properties of SZCY and BZCY Proton Conducting Ceramics for Hydrogen Production. *International Journal of Hydrogen Energy* **2017**, *42* (7), 3926–3937. https://doi.org/10.1016/j.ijhydene.2016.10.120.

(2) Deibert, W.; Ivanova, M. E.; Huang, Y.; Merkle, R.; Maier, J.; Meulenberg, W. A. Fabrication of Multi-Layered Structures for Proton Conducting Ceramic Cells. *Journal of Materials Chemistry A* **2021**, *00*, 1–12. https://doi.org/10.1039/d1ta05240c.

(3) Leonard, K.; Okuyama, Y.; Ivanova, M. E.; Meulenberg, W. A.; Matsumoto, H. Tailored and Improved Protonic Conductivity through Ba(ZxCe10−x)0.08Y0.2O3−δ Ceramics Perovskites Type Oxides for Electrochemical Devices. *ChemElectroChem* **2022**, *9* (4), 1–12. https://doi.org/10.1002/celc.202101663.

(4) Wang, N.; Toriumi, H.; Sato, Y.; Tang, C.; Nakamura, T.; Amezawa, K.; Kitano, S.; Habazaki, H.; Aoki, Y. La0.8Sr0.2Co1-XNi XO3-Δas the Efficient Triple Conductor Air Electrode for Protonic Ceramic Cells. *ACS Applied Energy Materials* **2021**, *4* (1), 554–563. https://doi.org/10.1021/acsaem.0c02447.

(5) Tang, W.; Ding, H.; Bian, W.; Wu, W.; Li, W.; Liu, X.; Gomez, J. Y.; Regalado Vera, C. Y.; Zhou, M.; Ding, D. Understanding of A-Site Deficiency in Layered Perovskites: Promotion of Dual Reaction Kinetics for Water Oxidation and Oxygen Reduction in Protonic Ceramic Electrochemical Cells. *Journal of Materials Chemistry A* **2020**, *8* (29), 14600–14608. https://doi.org/10.1039/d0ta05137c.

(6) Zhou, Y.; Liu, E.; Chen, Y.; Liu, Y.; Zhang, L.; Zhang, W.; Luo, Z.; Kane, N.; Zhao, B.; Soule, L.; Niu, Y.; Ding, Y.; Ding, H.; Ding, D.; Liu, M. An Active and Robust Air Electrode for Reversible Protonic Ceramic Electrochemical Cells. *ACS Energy Letters* **2021**, *6* (4), 1511–1520. https://doi.org/10.1021/acsenergylett.1c00432.

(7) Choi, S.; Davenport, T. C.; Haile, S. M. Protonic Ceramic Electrochemical Cells for Hydrogen Production and Electricity Generation: Exceptional Reversibility, Stability, and Demonstrated Faradaic Efficiency. *Energy and Environmental Science* **2019**, *12* (1), 206–215. https://doi.org/10.1039/c8ee02865f.

(8) Yoo, Y.; Lim, N. Performance and Stability of Proton Conducting Solid Oxide Fuel Cells Based on Yttrium-Doped Barium Cerate-Zirconate Thin-Film Electrolyte. *Journal of Power Sources* **2013**, *229*, 48–57. https://doi.org/10.1016/j.jpowsour.2012.11.094.

(9) Azimova, M. A.; McIntosh, S. On the Reversibility of Anode Supported Proton Conducting Solid Oxide Cells. *Solid State Ionics* **2011**, *203* (1), 57–61. https://doi.org/10.1016/j.ssi.2011.09.008.

(10) Huan, D.; Shi, N.; Zhang, L.; Tan, W.; Xie, Y.; Wang, W.; Xia, C.; Peng, R.; Lu, Y. New, Efficient, and Reliable Air Electrode Material for Proton-Conducting Reversible Solid Oxide Cells. *ACS Applied Materials and Interfaces* **2018**, *10* (2), 1761–1770. https://doi.org/10.1021/acsami.7b16703.

(11) Duan, C.; Kee, R.; Zhu, H.; Sullivan, N.; Zhu, L.; Bian, L.; Jennings, D.; O'Hayre, R. Highly Efficient Reversible Protonic Ceramic Electrochemical Cells for Power Generation and Fuel Production. *Nature Energy* **2019**, *4* (3), 230–240. https://doi.org/10.1038/s41560-019-0333-2.

(12) Lyagaeva, J.; Danilov, N.; Vdovin, G.; Bu, J.; Medvedev, D.; Demin, A.; Tsiakaras, P. A New Dy-Doped BaCeO3-BaZrO3 Proton-Conducting Material as a Promising

Electrolyte for Reversible Solid Oxide Fuel Cells. *Journal of Materials Chemistry A* **2016**, *4* (40), 15390–15399. https://doi.org/10.1039/c6ta06414k.

(13) He, F.; Song, D.; Peng, R.; Meng, G.; Yang, S. Electrode Performance and Analysis of Reversible Solid Oxide Fuel Cells with Proton Conducting Electrolyte of BaCe0.5Zr0.3Y0.2O3-δ. *Journal of Power Sources* **2010**, *195* (11), 3359–3364. https://doi.org/10.1016/j.jpowsour.2009.12.079.

(14) Kobayashi, T.; Kuroda, K.; Jeong, S.; Kwon, H.; Zhu, C.; Habazaki, H.; Aoki, Y. Analysis of the Anode Reaction of Solid Oxide Electrolyzer Cells with BaZr 0.4 Ce 0.4 Y 0.2 O 3- δ Electrolytes and Sm 0.5 Sr 0.5 CoO 3- δ Anodes . *Journal of The Electrochemical Society* **2018**, *165* (5), F342–F349. https://doi.org/10.1149/2.0891805jes.

(15) Ding, H.; Wu, W.; Jiang, C.; Ding, Y.; Bian, W.; Hu, B.; Singh, P.; Orme, C. J.; Wang, L.; Zhang, Y.; Ding, D. Self-Sustainable Protonic Ceramic Electrochemical Cells Using a Triple Conducting Electrode for Hydrogen and Power Production. *Nature Communications* **2020**, *11* (1). https://doi.org/10.1038/s41467-020-15677-z.

(16) Kim, J.; Jun, A.; Gwon, O.; Yoo, S.; Liu, M.; Shin, J.; Lim, T. H.; Kim, G. Hybrid-Solid Oxide Electrolysis Cell: A New Strategy for Efficient Hydrogen Production. *Nano Energy* **2018**, *44* (November 2017), 121–126. https://doi.org/10.1016/j.nanoen.2017.11.074.